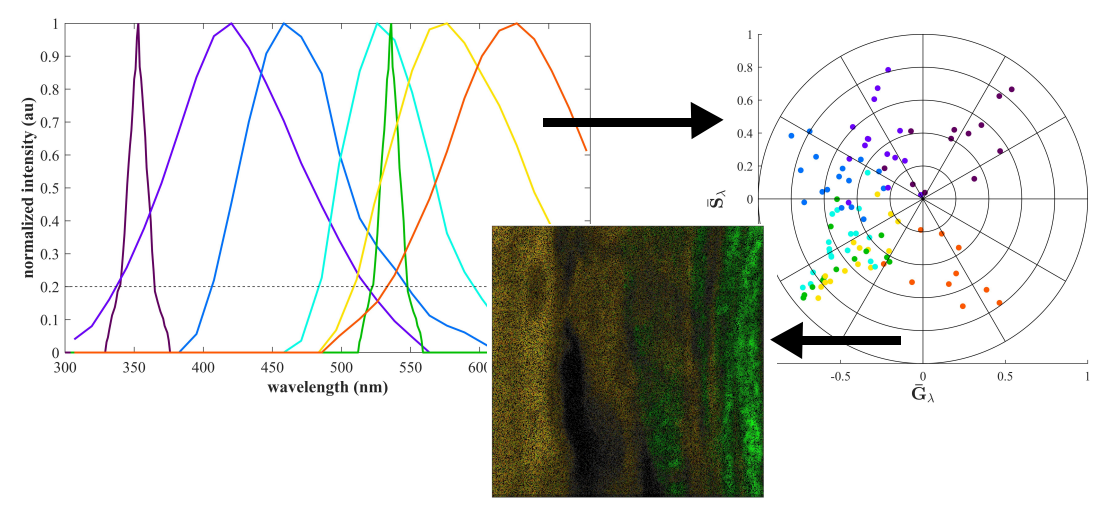
Chemical complexity of the retina addressed by novel phasor analysis of unstained multimodal microscopy

Jessica Kline, Marcos Dantus

Department of Chemistry, Michigan State University, East Lansing MI 48824

Graphic Abstract:



Highlights:

- Novel phasor analysis for hyperspectral analysis of more than three components
- Quantitative spectral unmixing of seven retina fluorophores
- Accurate unmixing of components with highly overlapped spectra

ABSTRACT

Unstained multimodal microscopy is capable of non-invasively obtaining chemically specific information with sub-micron spatial resolution; however, spectral overlap makes quantitative analysis difficult. Here, multimodal images that include second-harmonic generation, third-harmonic generation, and two- and three-photon excited fluorescence signals from unstained retinas are analyzed. The composition from each layer of the retina is determined using a novel variation of phasor analysis that is not limited to three components. The super-phasor unmixing (SPU) method is compared with fully constrained linear spectral unmixing. The seven spectroscopic signals in the spectral range 300-690 nm enable the quantitative unmixing of sub-micron pixel spectra even in the presence of noise. The performance of SPU was found to be significantly superior to linear unmixing especially in regions of high spectral overlap. The analysis being presented represents an important step in addressing chemical complexity in congested spaces with applicability to biomedical imaging and unmixing of hyperspectral images.

KEYWORDS: biomedical imaging, nonlinear spectroscopy, analytical chemistry, hyperspectral image analysis

Over the last three decades, multiphoton microscopy has emerged as a high-resolution imaging technique that provides many advantages over confocal microscopy, especially for depth resolved imaging [1–3]. The quality of multiphoton microscopy has been significantly improved as lasers

with longer wavelengths and shorter pulses have been developed. At wavelengths longer than 850 nm, the maximum absorption of DNA is no longer accessible via three-photon excitation preventing three-photon induced DNA damage [4]. Three-photon excitation at 1070 nm produces images with greater contrast and resolution than two-photon excitation at 800 nm [5]. Shorter pulses require lower pulse energies leading to decreased thermal damage to achieve the same peak intensity and signal level of a longer pulses [6]. Thus, short pulses enable imaging of highly absorptive tissues that are highly sensitive to photodamage [7]. Although multiphoton microscopy was originally reliant on fluorescently stained tissues, there have been many developments focused on moving toward non-invasive and unstained imaging that takes advantage of the native fluorophores in tissues. Multimodal imaging typically includes the collection of second harmonic generation (SHG) and third harmonic generation (THG) from samples, as well as two- and threephoton excitation fluorescence [8]. SHG requires non-centrosymmetric molecules, and in most tissues indicates the presence of collagen, while THG requires a change in the index of refraction at the focal spot, which typically occurs in the presence of lipid layers in tissue. While autofluorescence is commonly used to identify broad molecular types and is used in medical diagnoses, a quantitative analysis of chemicals by multiphoton microscopy is complex [9–12]. Autofluorescent molecules in a biological tissue often have closely overlapped spectra, which poses a significant challenge for quantitative analysis. Solving the challenge of chemical complexity via non-invasive imaging could open novel diagnostic methods where subtle chemical transformations can signal disease or identify the presence of a pathogen.

The images used for analysis here correspond to multimodal images of fixed mouse retinas that have been described in an earlier publication by our group, which includes details about the retina preparation [13]. That study showed fluorescence spectra and lifetime data from different retinal layers, although no spectral unmixing was attempted. Additional details about the images and their acquisition are given in the Methods section.

We used a phasor-based analysis because it compresses the spectra from a pixel or voxel (in depth resolved imaging) into a single point, and that point's position provides the percent contribution of each component. The phasor-based analysis method is a modeless approach for describing lifetime and spectral data acquired from cuvette and microscopy experiments. The mathematical relationships were derived by Weber, while Jameson et al. first introduced the phasor plots [14,15]. Each spectrum $I_i(\lambda)$ is transformed to phasor coordinates (G_i and S_i), according to eqs 1 and 2 [16]. The maximum and minimum wavelengths of the spectral window of interest are λ_{\min} and λ_{\max} .

$$G_{i} = \frac{\int_{\lambda_{\min}}^{\lambda_{\max}} I_{i}(\lambda) \cos\left(\frac{2\pi(\lambda - \lambda_{\min})}{\lambda_{\max} - \lambda_{\min}}\right) d\lambda}{\int_{\lambda_{\min}}^{\lambda_{\max}} I_{i}(\lambda) d\lambda}$$
(1)

$$S_{i} = \frac{\int_{\lambda_{\min}}^{\lambda_{\max}} I_{i}(\lambda) \sin\left(\frac{2\pi(\lambda - \lambda_{\min})}{\lambda_{\max} - \lambda_{\min}}\right) d\lambda}{\int_{\lambda_{\min}}^{\lambda_{\max}} I_{i}(\lambda) d\lambda}$$
(2)

Eqs 1 and 2 correspond to cosine and sine transforms of the spectrum that, when plotted in the phasor unit circle, convert a complex spectrum into a single point. One can also consider these formulas as a measurement of the overlap between the spectrum described by $I(\lambda)$ and a cosine or

sine function (Eq. 1 or 2) with the period defined by the spectral range of λ_{max} and λ_{min} . The resulting G and S coordinates are referred to here as the phasor corresponding to that spectrum. Each point in the phasor plot has an associated magnitude and angle. As the central wavelength (defined as the center of mass, not the wavelength of maximum intensity) of the spectrum increases a phasor point moves counterclockwise, and as the spectral bandwidth increases the phasor moves towards the origin. Note that the spectrum does not need to be Gaussian; it can have any shape. Phasors, like Fourier transforms, are bound by linear combinations, such that a phasor representing a mixed spectrum will fall on the line joining the phasors corresponding to the two pure compounds or within the area encompassed by the phasors of three pure components. Mixed phasors can be solved for up to three components using Eq. 3 [16].

$$S_i = aS_a + bS_b + cS_c$$

$$G_i = aG_a + bG_b + cG_c$$

$$a + b + c = 1$$
(3)

where the spectrum obtained for a given pixel can be decomposed into the percentages (a, b, c) of up to three components with the associated phasor coordinates S_a , S_b , S_c , G_a , G_b , G_c . The power of phasor analysis is contained in Eq. 3, which implies that the position of a phasor in the phasor plot solves the algebraic equation describing the contributions of the three components to the measured spectrum. As such, phasor analysis can be used for spectral unmixing. It should be emphasized that Eq. 3 does not solve for the emitter absolute concentration but instead solves for the percent emissive contribution of each fluorophore.

The analysis described here identifies the percent composition of seven retinal fluorophores and harmonophores: third harmonic generation (THG), second harmonic generation (SHG), elastin, nicotinamide adenine dinucleotide (NADH), flavin adenine dinucleotide (FAD), melanin, and di-retinoid-pyridinium-ethanolamine (A2E). To achieve the analysis of more than three components, we developed a sectional approach to phasor analysis described below. The spectra of these seven contributors are shown in Fig. 1a and their respective phasors are shown in Fig. 1b. The fluorescence spectra of the seven contributors were obtained by placing solutions of each pure fluorophore at the focal point of the microscope objective, exciting with the Yb-fiber laser and collecting the resulting emission spectra with the PMT used in the experiment.

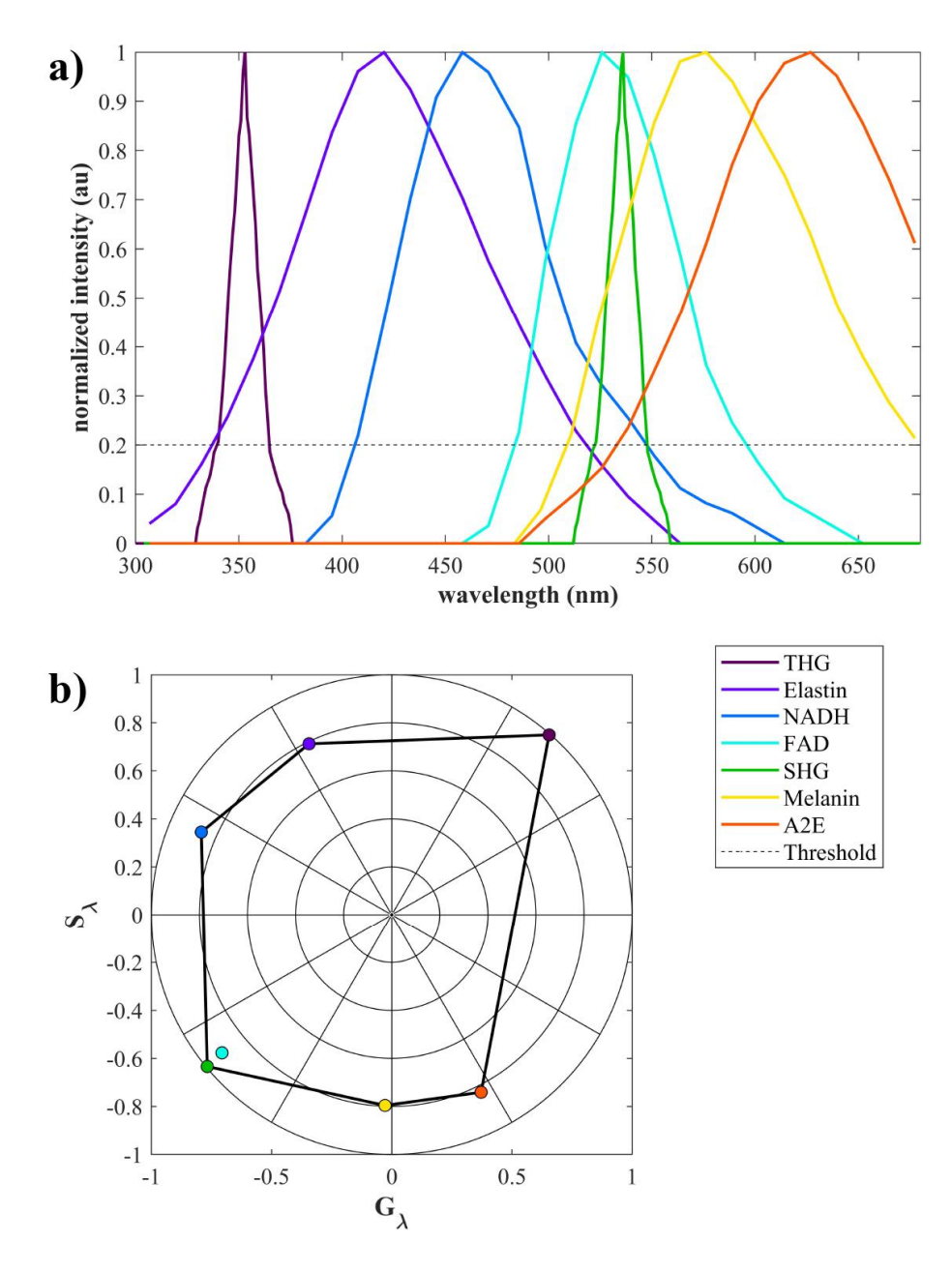


Figure 1. a) Spectra of seven contributing components with analysis relevant intensity threshold indicated. **b)** Phasor plot of each of the seven components shown in (a) over the range 300 nm to 686 nm. (1.5 column)

Phasor-based spectral contribution analysis is limited to three components because of the two-dimensionality of the phasor plot [16]. Therefore, if four or more emitters contribute to a spectrum the phasor approach is not valid. However, here we present a method for analyzing a significantly greater number of components. In order to expand the method, the contributing spectra were split into pairs or triads of emitters over ranges where they could be reasonably considered the only emitters, and their relative contributions were determined using Eq. 3. NADH and elastin were identified via phasors between 380 and 490 nm, see Fig. 2a. FAD, SHG and

melanin were related via phasors between 490 and 550 nm, see Fig. 2b. Melanin and A2E were related via phasors between 550 and 690 nm, see Fig. 2c. In each case the red dot represents the spectrum for which contributions are being solved for. Super phasor unmixing (SPU) analysis is described by Eq. 4, where the super phasor coordinates \bar{S}_k and \bar{G}_k are given by sums of phasors, S_e , S_f , S_g , G_e , G_f , G_g , each one containing up to three contributors. Note that SPU could be taken one additional step, such that super phasors can be constructed from a set of super phasors.

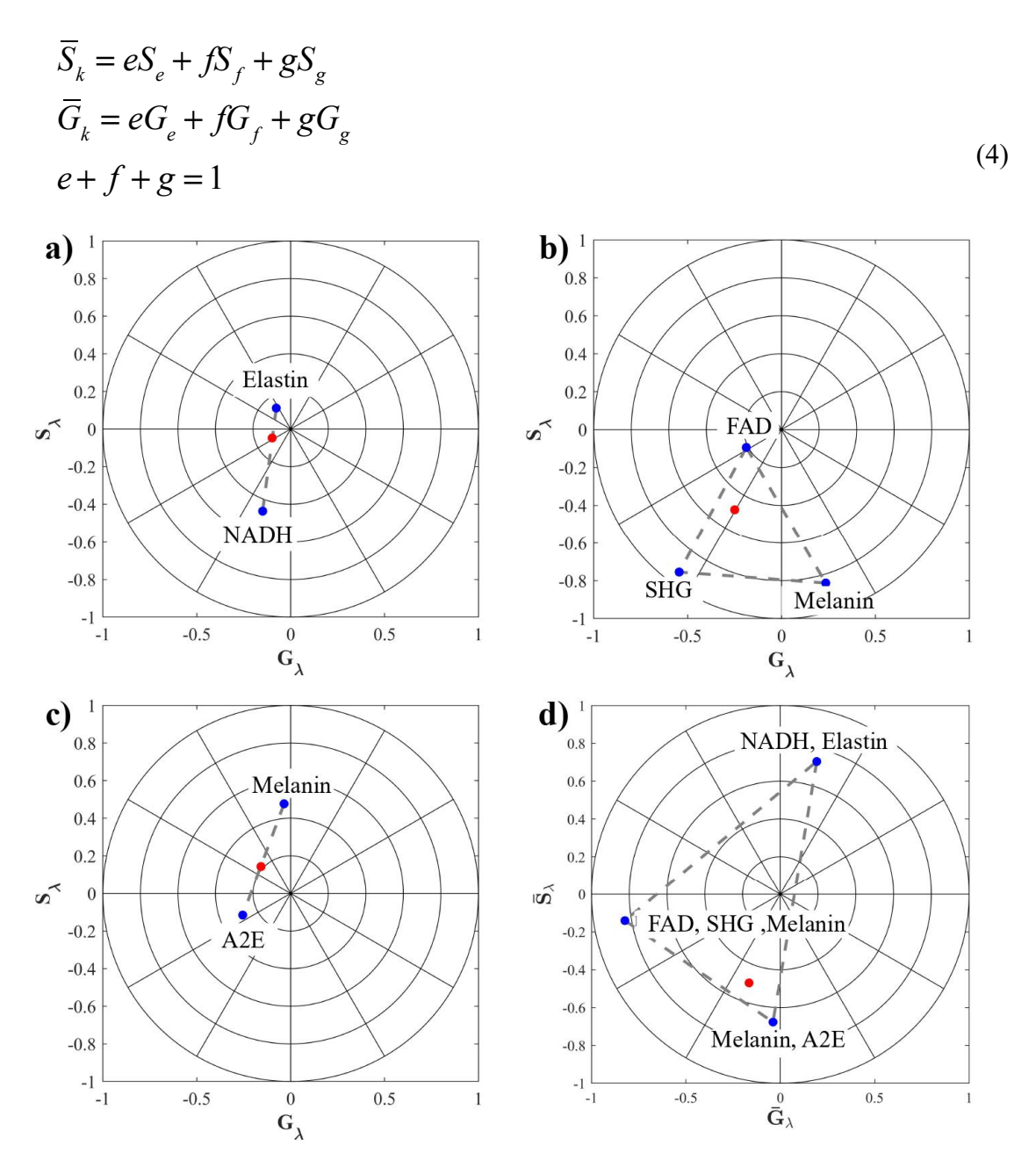


Figure 2. Sample sectional and super phasor plots **a)** NADH and elastin sectional phasor plot over the range of 380 to 490 nm **b)** FAD, SHG and melanin sectional phasor plot over the range of 490 to 550 nm. **c)** melanin and A2E sectional phasor plot over the range of 550 to 690 nm **d)** Super phasor plot constructed from the representative phasors

from the three sectional phasor plots over the range of 380 to 690 nm. In each figure the red dot represents the spectrum for which contributions are being solved for. (Two column)

Equation 5 illustrates the application of Eq. 4 to the super phasor plot shown in Fig 2d. Here the values of e,n,f,h,m_1,m_2 and a correspond to the percent contributions of elastin, NADH, FAD, SHG, melanin and A2E, respectively, from the application of Eq. 3 to the sectional phasor plots of Figs 2a-c. The values obtained from these equations can be combined to find the total percentage of the fluorescence spectrum represented by each component. For instance, the total percent contribution of elastin is equal to $x \cdot e$. The solutions from Fig. 2d were combined with the THG contribution, which was determined directly by integration because its spectrum does not overlap with the other components, and the sum was normalized to 1 to find the percent contributions of the seven components.

$$\overline{S}_{\lambda} = x \left(eS_{elastin} + nS_{NADH} \right) + y \left(fS_{FAD} + hS_{SHG} + m_1 S_{melanin} \right) + z \left(aS_{A2E} + m_2 S_{melanin} \right)
\overline{G}_{\lambda} = x \left(eG_{elastin} + nG_{NADH} \right) + y \left(fG_{FAD} + hG_{SHG} + m_1 G_{melanin} \right) + z \left(aG_{A2E} + m_2 G_{melanin} \right)
x + y + z = 1$$
(5)

While the phasor plots shown in Fig. 2 indicate the percent total emissive contributions of each of the different emitters, they also indicate that the correct fluorophores are being analyzed. If the spectrum being analyzed contained an emission from a fluorophore that is not part of the seven emitters being considered, the resulting phasor (red dot) of that spectrum would be located outside of the space defined by contributing fluorophores, represented in Fig. 2 by the gray dashed lines connecting the blue fluorophore phasors, or by the area inside the triangle (as in Fig. 2b).

The validity of phasor based unmixing for two to three compounds has been previously addressed in detail [16]. However, the validity of SPU presented here to determine the percent composition of more than three species requires quantitative proof. We tested SPU by analyzing 100 spectra created by combining the emissions shown in Fig. 1 with random but known concentrations. These spectra were then analyzed via SPU. The comparison between the known and the retrieved concentrations was then plotted for the same set of spectra analyzed with different noise levels. The results from these comparisons are shown in Fig. 3. In the noiseless example, Fig. 3a, SPU returned concentrations within 0.2% of the actual concentration. In the typical case, when noise in the spectrum is 5%, shown in Figure 3b, the retrieved concentrations were within 2% of actual values. When 25% noise was used, corresponding to very low signals, SPU, shown in Figure 3c, retrieved concentrations within 7% of the actual value. The phasor plot of the spectra used to construct these correlation plots is shown Fig. 3d. These results show that linear combinations, as defined in Eq. 3 apply to SPU and imply Eq. 4 is valid. We find that relatively low error values can be expected from this type of analysis.

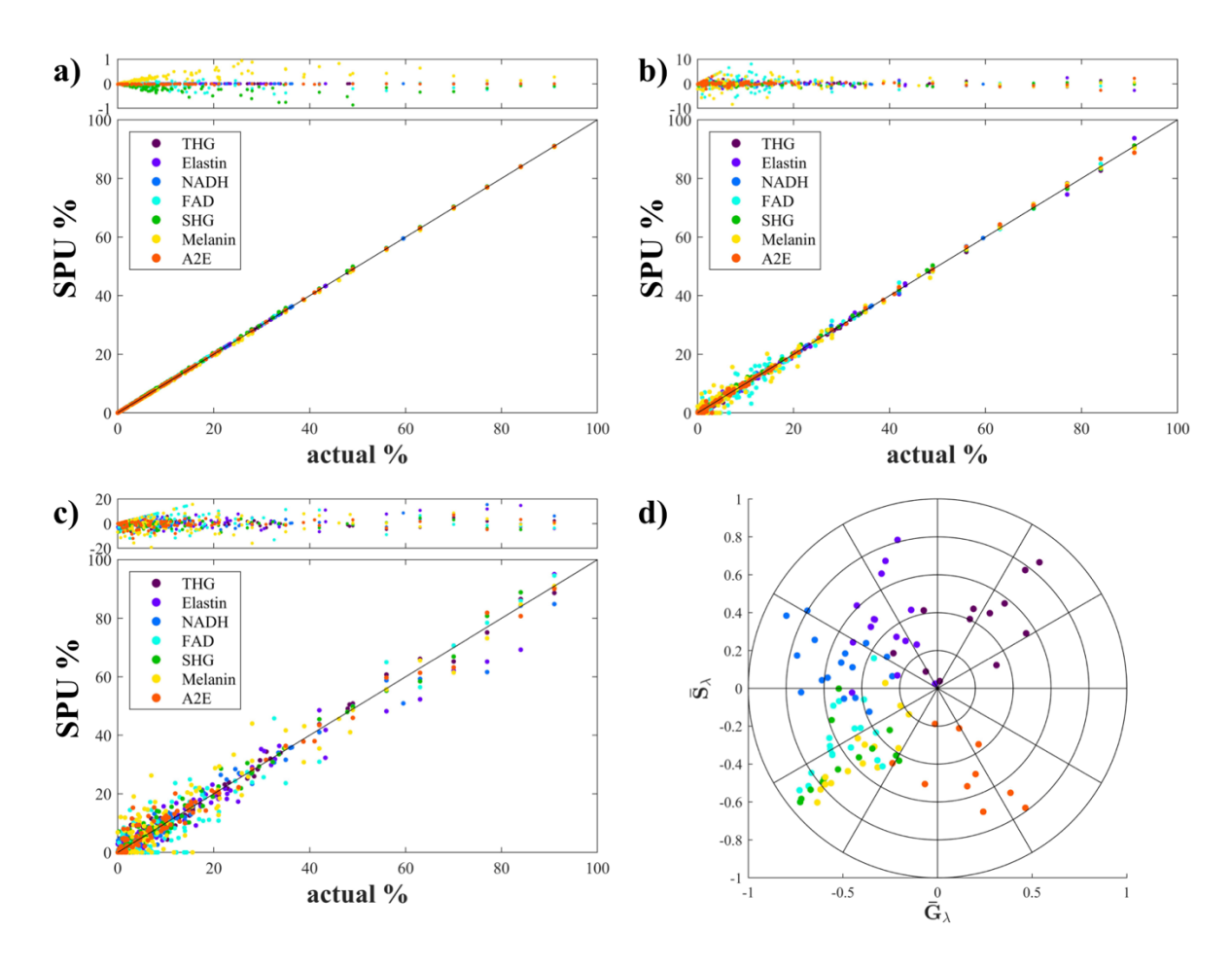


Figure 3. Correlation between the actual concentration and the SPU determined concentrations with the residual shown on top for spectral data with **a)** no noise **b)** 5% noise **c)** 25% noise **d)** super-phasor plot of spectra used for the correlation plots, colored by maximum contributor. (Two column)

Each layer of the retina - nerve fiber layer (NFL), ganglion cell layer (GCL), inner plexiform layer (IPL), inner nuclear layer (INL), outer plexiform layer (OPL), outer nuclear layer (ONL), inner receptor layer (IRL), outer receptor layer (ORL), retinal pigment epithelium (RPE), choroid and sclera - has a characteristic emission spectrum shown in Fig. 4. Each spectrum shown in Fig. 4 was processed via SPU, which results in the relative percentages for each identified compound. The percentages represented correspond to the total emissive contribution to the signal but do not represent the absolute concentrations of components. Obtaining absolute concentrations would require taking into account parameters such as fluorescence quantum yield, two and three photon cross sections, and second and third order susceptibilities, which are not taken into account here. Factors such as these can be taken into account after SPU and do not affect the analysis process presented here.

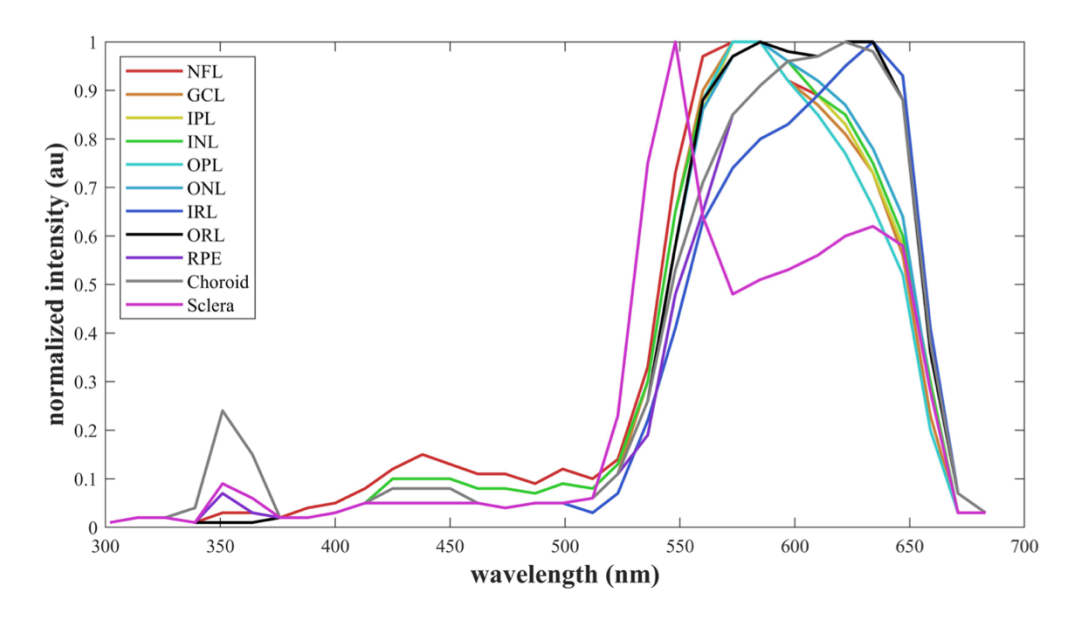


Figure 4. Characteristic fluorescence emission spectra of each retinal layer. (Two column)

The relative percentages, as found via SPU, are shown for each layer in Fig. 5. The most anterior layers (NFL – ONL) have near constant percent contributions with approximately equal amounts of melanin and A2E. The more proximal retinal layers (IRL – Choroid) see a slight increase in the percent of A2E present, while melanin contributions remain relatively constant. After maximum A2E contributions in the IRL, A2E levels drop with movement towards the posterior. The Sclera is the only layer identified as having significant contributions from SHG and also contains the least A2E of any layer. FAD, NADH and elastin levels remain relatively constant across all layers, while THG, primarily arising from lipids, is only found in the three most posterior layers (RPE, Choroid and Sclera).

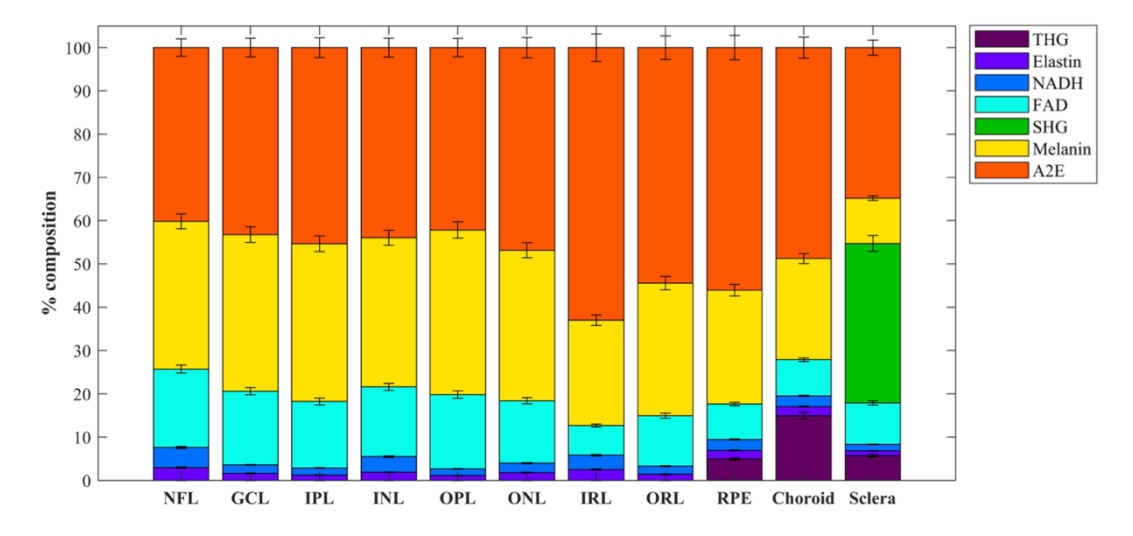


Figure 5. Relative percent composition of retinal layers as determined by SPU. (Two column)

While SPU is proposed here as a new method for spectral unmixing in congested spectral data, there are a variety of methods in use currently for the same purpose [17]. Figure 6 shows the unmixing of the retinal layers analyzed here as determined by fully constrained linear spectral unmixing (FCLSU) [18]. SPU and FCLSU are in good agreement for THG and SHG contributions. They are in relative agreement for elastin and NADH, although FCLSU tends to assign slightly more of the spectrum to these to contributors, approximately 7% combined, than SPU, approximately 4% combined. SPU and FCLSU return significantly different contribution values for FAD. FCLSU only finds FAD in the Sclera, while SPU finds FAD throughout the retina. The two analysis methods also return significantly different values for melanin and A2E. FCLSU only finds A2E in the posterior layers (IRL-Sclera), while SPU finds A2E throughout the retinal layers. Even when FCLSU does find A2E, the contributions are nearly half of the contributions found by SPU in the same retinal layers.

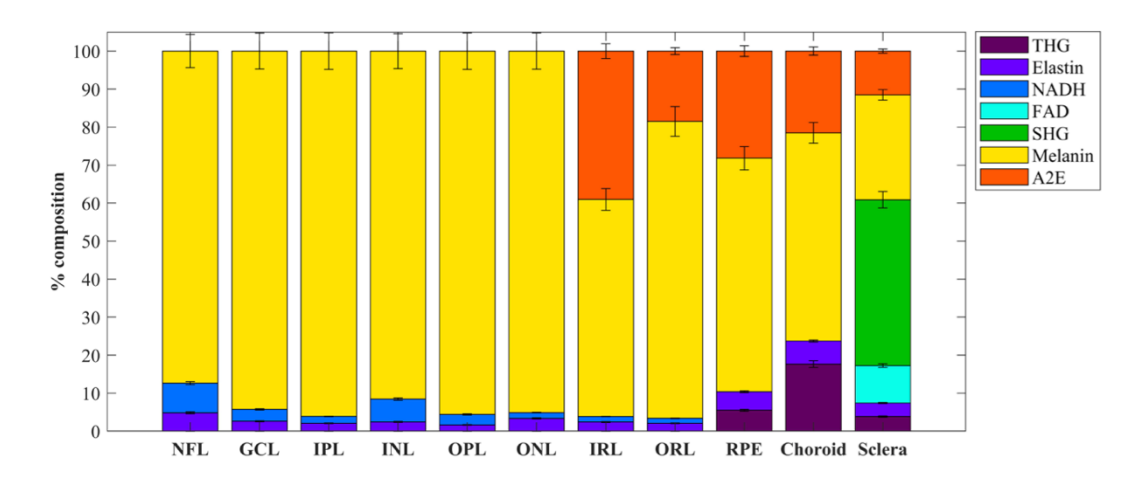


Figure 6. Relative percent composition of retinal layers as determined by FCLSU. (Two column)

Given differences found by SPU and FCLSU, we set out to quantitatively compare the two methods using the same 100 spectra, where the concentration of each of the seven components were varied randomly from 0-100%. Each of the resulting mixed spectra was then unmixed by SPU and FCLSU. The difference between the known and returned percentages was calculated and the standard deviation of that difference is reported in Table 1. At the low noise level of 0.1%, we found that both SPU and FCLSU returned composition values within 0.2% of the actual values. At 5% noise SPU and FCLSU have similar standard deviations for THG and SHG, which are the two easiest components to identify. However, for the other five components FCLSU standard deviations are 1.6 to 3.4 times larger than SPU standard deviations. When noise was 25% FCLSU standard deviations are between 1.3 and 2.7 times larger than those retrieved by SPU for all components except for SHG.

Table 1. Quantitative assessment of the SPU and FCLSU methods under three different noise levels. The standard deviation of the difference between the actual and calculated percent composition in the simulated seven-component

spectra are given for both methods.

Noise	Analysis	Standard Deviation of the Difference in Percentage						
Level	Method	THG	Elastin	NADH	FAD	SHG	Melanin	A2E
0.1%	SPU	0.012	0.015	0.014	0.13	0.17	0.21	0.018
	FCLSU	0.014	0.029	0.044	0.13	0.015	0.15	0.049
5%	SPU	0.51	0.84	0.55	1.9	0.62	1.8	0.62
	FCLSU	0.58	1.5	1.9	3.0	0.60	3.2	1.6
25%	SPU	1.8	2.9	2.2	6.9	2.6	6.8	2.6
	FCLSU	2.5	5.7	5.9	9.1	2.7	11.6	6.5

Figure 7 shows the comparison between the performance of SPU and FCLSU at a 5% noise level. The returned percent compositions were separated into 10 bins, each with a 10% composition width. The same separation was performed on the spectra's known percent compositions. Each bin was normalized to the number of known occurrences of that percent composition. Figure 7a shows the difference between the actual and retrieved number for each bin and unmixing method. Values close to zero indicate that a method is accurate at quantifying compositions in that bin range. In all 10 bins SPU was found to be more accurate than FCLSU. In the three bins covering compositions between 30 and 60 percent, SPU matches the known counts perfectly. While both methods are less accurate at compositions of over 60%, those values are only significant in two or three component systems because as the number of components in a system increases it becomes much less likely for any single component to make up a large percentage of the spectrum. Thus, the bins between 0 and 50 percent are much more indicative of these methods performances in unmixing many component spectra. Across this key range, SPU is nearly ten times more accurate than FCLSU. Figure 7b compares the FCLSU determined percent compositions to the actual percent compositions for seven-component data with 5% noise. The comparison of figures 3b and 7b shows the residual has a factor of 2 larger y-axis to accommodate the larger deviation from FCLSU.

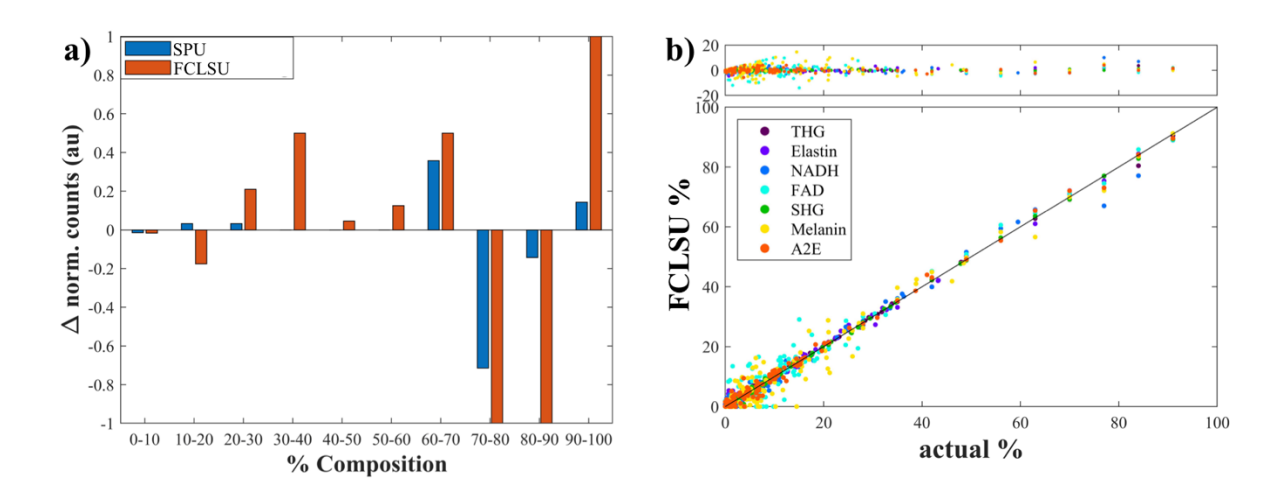


Figure 7. FCLSU and SPU performance on theoretical spectra a) Comparison between SPU and FCLSU for a 5% noise spectral data. b) Correlation between FCLSU determined percent compositions and actual percent compositions in a 5% noise spectral data.

By comparing the data presented in Figs. 5-7 and Table 1, the advantages of SPU over other spectral unmixing methods become apparent. SPU is significantly better at distinguishing components with large spectral overlap, such as, FAD, SHG, melanin and A2E. FCLSU performs similarly to SPU in the significantly less congested 300 to 450 nm range. However, in the more congested 500 to 700 nm range FCLSU struggles to accurately quantify contributions.

SPU can also be applied to each pixel in an image or each voxel in a depth resolved image. In this way, an image collected via unstained multimodal microscopy can be colored according to the main contributors at each pixel. Figure 8 shows one such image. The composition of each pixel, and its corresponding color, was determined via the same percent analysis as the retinal layers. This analysis shows a clear shift in the major spectral contributors in the image. The left-hand side of the image has significant A2E and melanin contributions. However, the right-hand side of the image sees major contributions from SHG.

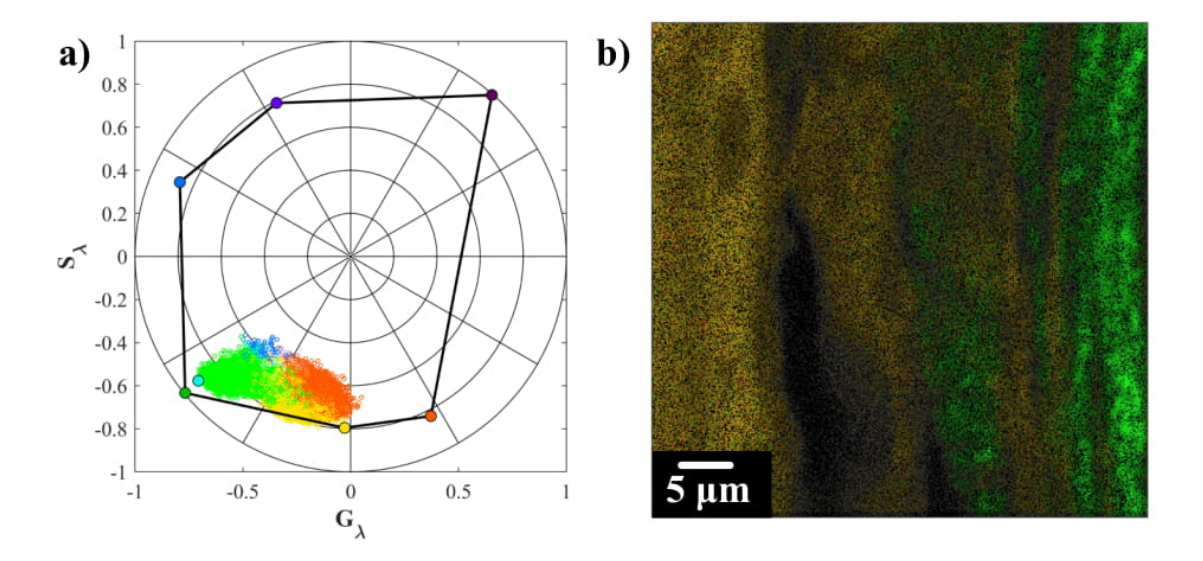


Figure 8. Multimodal microscopy image of the RPE, Choroid, and Sclera (from left to right) analyzed using super phasors **a)** Colorized phasor plot of the image over the range 300 to 686 nm **b)** Phasor plot colored microscopy image. The color of each pixel was determined by the maximum contributor found by SPU. (Two column)

In conclusion, here we have introduced the method SPU for analyzing complex chemical information in biomedical images. This method allows the reliable unmixing of multiple emitters, as shown by the seven components separated here. This method has great potential for distinguishing contributors across complex systems where various emitters are within close proximity to each other, demonstrated here for the retina. It has also been demonstrated that SPU performs better in congested spectral data than the FCLSU method used for hyperspectral analysis [18]. SPU also provides a quantitative method that can be used to track small changes in the chemical make-up of a system.

EXPERIMENTAL METHODS

The custom designed laser source for our multiphoton microscope is a Yb-fiber laser oscillator producing pulses with sub-40 fs pulse durations (full-width half-maximum) (1.07 µm,

42 MHz) [19]. The microscope used was a Nikon TE2000 in the inverted configuration. For imaging, a 40x water immersion objective was employed with a working distance of 0.5 mm (Zeiss LD-C APOCHROMAT 1.1NA, Jena, Germany) to focus the beam on the retina to a beam waist (diameter of the beam at the focus) of $\sim 0.5 \mu m$, allowing the generation of peak intensities high enough to induce multiphoton processes with less than 7 mW of average power and pulse durations of 38 ± 1 fs. Thus, minimizing the effects of photobleaching and thermal damage. Laser scanning was done with galvanometer mirrors. The peak intensity was maximized through the use of a pulseshaper (MIIPS HD, BioPhotonic Solutions Inc., East Lansing, MI, USA) to compensate for the high-order dispersion of the objective [20-22]. Signal detection was accomplished in the epidirection with two separate detection systems. Although the epi direction is not ideal for THG collection, the light which we have identified as THG matches in position, bandwidth and lifetime to THG. To obtain frequency and time-resolved data a time-correlated single photon-counting (TCSPC) system with a compact spectrometer and a 16-photomultiplier tube (PMT) array were used (SPC-830 TCSPC, Becker-Hickl, GmBH). The spectral resolution of the TCSPC system is ~12.5 nm, limited by the physical size of each anode in the 16-annode PMT and confirmed with a mercury lamp. The grating in the spectrometer was rotated to select different spectral regions. Here two grating positions were used to collect the fluorescence spectra; one with a collection range from ~300 nm to ~500 nm and the other from ~480 nm to ~680 nm. The images of the retinas obtained using the TCSPC were imaged with 6.9 mW of power or less for a total exposure time of 3 minutes (90 seconds per grating position). The type and preparation for the mouse retinas is described in Ref. 13.

ASSOCIATED CONTENT

Supporting information

Describe if any:

AUTHOR INFORMATION

Corresponding Author

*Address: Chemistry Building, 578 S. Shaw Lane, Michigan State University, East Lansing, MI 48824. E-mail: dantus@msu.edu.

DECLATATION OF COMPETING INTEREST

The authors declare that they have no known competing financial interests or personal relationships that could have appeared to influence the work reported in this paper.

ACKNOWLEDGMENTS

This work was supported by the National Science Foundation Grant CHE1836498, JK is grateful for REU funding through this grant. The retinal images that were used for the phasor analysis were obtained by Gabrielle Murashova a few years ago in our research group. Those figures were part of an earlier publication.

REFERENCES

- [1] W. Denk, J.H. Strickler, ; Watt, W. Webb, Two-Photon Laser Scanning Fluorescence Microscopy, 1990.
- [2] P.T.C. So, C.Y. Dong, B.R. Masters, K.M. Berland, Two-Photon Excitation Fluorescence Microscopy, Annu. Rev. Biomed. Eng. 2 (2000) 399–429.

- https://doi.org/10.1146/annurev.bioeng.2.1.399.
- [3] K. Koenig, Hybrid multiphoton multimodal tomography of in vivo human skin, IntraVital. 1 (2012) 11–26. https://doi.org/10.4161/intv.21938.
- [4] S.N. Arkhipov, I. Saytashev, M. Dantus, Intravital Imaging Study on Photodamage Produced by Femtosecond Near-infrared Laser Pulses In Vivo, Photochem. Photobiol. 92 (2016) 308–313. https://doi.org/10.1111/php.12572.
- [5] B. Nie, I. Saytashev, M. Dantus, Towards a compact fiber laser for multimodal imaging, in: Springer Proc. Phys., 2015. https://doi.org/10.1007/978-3-319-13242-6_182.
- [6] P. Xi, Y. Andegeko, L.R. Weisel, V. V. Lozovoy, M. Dantus, Greater signal, increased depth, and less photobleaching in two-photon microscopy with 10 fs pulses, Opt. Commun. 281 (2008) 1841–1849. https://doi.org/10.1016/j.optcom.2007.09.066.
- [7] I. Saytashev, R. Glenn, G.A. Murashova, S. Osseiran, D. Spence, C.L. Evans, M. Dantus, Multiphoton excited hemoglobin fluorescence and third harmonic generation for non-invasive microscopy of stored blood, Biomed. Opt. Express. 7 (2016) 3449. https://doi.org/10.1364/boe.7.003449.
- [8] H. Tu, Y. Liu, D. Turchinovich, M. Marjanovic, J.K. Lyngsø, J. Lægsgaard, E.J. Chaney, Y. Zhao, S. You, W.L. Wilson, B. Xu, M. Dantus, S.A. Boppart, Stain-free histopathology by programmable supercontinuum pulses, Nat. Photonics. 10 (2016) 534–540. https://doi.org/10.1038/nphoton.2016.94.
- [9] R.W. Young, D. Bok, Participation of the retinal pigment epithelium in the rod outer segment renewal process., J. Cell Biol. 42 (1969) 392–403. https://doi.org/10.1083/jcb.42.2.392.
- [10] M.L. Katz, W.L. Stone, E.A. Dratz, Fluorescent pigment accumulation in retinal pigment epithelium of antioxidant-deficient rats, Investig. Ophthalmol. Vis. Sci. 17 (1978) 1049–1058.
- [11] S. Huang, A.A. Heikal, W.W. Webb, Two-photon fluorescence spectroscopy and microscopy of NAD(P)H and flavoprotein, Biophys. J. 82 (2002) 2811–2825. https://doi.org/10.1016/S0006-3495(02)75621-X.
- [12] M.C. Skala, K.M. Riching, A. Gendron-Fitzpatrick, J. Eickhoff, K.W. Eliceiri, J.G. White, N. Ramanujam, In vivo multiphoton microscopy of NADH and FAD redox states, fluorescence lifetimes, and cellular morphology in precancerous epithelia, Proc. Natl. Acad. Sci. U. S. A. 104 (2007) 19494–19499. https://doi.org/10.1073/pnas.0708425104.
- [13] G.A. Murashova, C.A. Mancuso, J.L. Canfield, S. Sakami, K. Palczewski, G. Palczewska, M. Dantus, Multimodal nonlinear optical imaging of unstained retinas in the epi-direction with a sub-40 fs Yb-fiber laser, Biomed. Opt. Express. 8 (2017) 5228. https://doi.org/10.1364/boe.8.005228.
- [14] G. Weber, Resolution of the fluorescence lifetimes in a heterogeneous system by phase and modulation measurements, J. Phys. Chem. 85 (1981) 949–953. https://doi.org/10.1021/j150608a006.
- [15] D.M. Jameson, E. Gratton, R.D. Hall, The measurement and analysis of heterogeneous emissions by multifrequency phase and modulation fluorometry, Appl. Spectrosc. Rev. 20 (1984) 55–106. https://doi.org/10.1080/05704928408081716.
- [16] F. Fereidouni, A.N. Bader, H.C. Gerritsen, Spectral phasor analysis allows rapid and reliable unmixing of fluorescence microscopy spectral images, Opt. Express. 20 (2012) 12729. https://doi.org/10.1364/oe.20.012729.
- [17] X. Ceamanos, S. Valero, Processing Hyperspectral Images, in: Opt. Remote Sens. L. Surf.

- Tech. Methods, Elsevier Inc., 2016: pp. 163–200. https://doi.org/10.1016/B978-1-78548-102-4.50004-1.
- [18] C. Shi, L. Wang, Incorporating spatial information in spectral unmixing: A review, Remote Sens. Environ. 149 (2014) 70–87. https://doi.org/10.1016/j.rse.2014.03.034.
- [19] B. Nie, D. Pestov, F.W. Wise, M. Dantus, Generation of 42-fs and 10-nJ pulses from a fiber laser with self-similar evolution in the gain segment, Opt. Express. 19 (2011) 12074. https://doi.org/10.1364/oe.19.012074.
- [20] Y. Coello, V. V. Lozovoy, T.C. Gunaratne, B. Xu, I. Borukhovich, C. Tseng, T. Weinacht, M. Dantus, Interference without an interferometer: a different approach to measuring, compressing, and shaping ultrashort laser pulses, J. Opt. Soc. Am. B. 25 (2008) A140. https://doi.org/10.1364/josab.25.00a140.
- [21] V. V. Lozovoy, I. Pastirk, M. Dantus, Multiphoton intrapulse interference IV Ultrashort laser pulse spectral phase characterization and compensation, Opt. Lett. 29 (2004) 775. https://doi.org/10.1364/ol.29.000775.
- [22] P. Xi, Y. Andegeko, D. Pestov, V. V. Lovozoy, M. Dantus, Two-photon imaging using adaptive phase compensated ultrashort laser pulses, J. Biomed. Opt. 14 (2009) 014002. https://doi.org/10.1117/1.3059629.